UNIVERSITY OF CALIFORNIA,
IRVINE

Constructing a Fluorescence Lifetime Nanoprobe Library to Advance Lifetime-Based Multiplexing

THESIS

submitted in partial satisfaction of the requirements
for the degree of

MASTER OF SCIENCE

in Biomedical Engineering

by

Louis Mejia

Thesis Committee:
Assistant Professor Jered B. Haun, Chair
Associate Professor James P. Brody
Assistant Professor Michelle A. Digman

2019

DEDICATION

For Kairie.

TABLE OF CONTENTS

LIST OF FIGURES

Page

LIST OF ABBREVIATIONS

Variable Name	Description
ATCC	American Type Culture Company
Az	Azide
BP	Backfill PEGylation
BSA	Bovine Serum Albumin
CEST	Carboxyethylsilanetriol
COOH	Carboxylic Acid
DBCO	4-Dibenzocyclooctyne
DLS	Dynamic Light Scattering
DMF	Dimethylformamide
EDC	N-(3-Dimethylaminopropyl)-N-ethylcarbodiimide Hydrochloride
EpCAM	Epithelial Cell Adhesion Molecule
FLIM	Fluorescence Lifetime Imaging Microscopy
HER2	Human Epidermal Growth Factor Receptor 2
IC	Immunoconjugate
MeTz	Methyltetrazine
NHS	N-Hydroxysuccinimide
PBS	Phosphate Buffered Saline
PBS+	PBS with BSA
PEG	Polyethylene Glycol
PQY	Pseudo Quantum Yield
QD	Quantum Dot
SEC	Size Exclusion Chromatography
SEM	Scanning Electron Microscopy
TCO	Trans-cyclooctene
TEM	Transmission Electron Microscopy
TEOS	Tetraethyl Orthosilicate
TPMP	3-(trihydroxysilyl)propyl Methylphosphonate

ACKNOWLEDGMENTS

I would like to express my utmost gratitude for Dr. Jered Haun, for his unrelenting support, guidance, and belief in my success. None of this would have been possible without him. I would also like to thank Dr. James Brody and Dr. Michelle Digman for their valuable time and insight as a part of my committee. I would like to show appreciation towards Ashwin Kainkaryam and Dr. Rajesh Kota for their guidance in the early stages of this project, and to Xi Chen and Minseok Kwak for their help in expanding our work. I would also like to thank Lauren Lastra, Juliana de Carvalho, Nora Mohammad, and Samantha Sanchez for all their assistance, and to Dr. Maha Rahim, Vanessa Herrera, and Hauna Krekemeyer for their help and guidance.

I would like to also acknowledge project funding in part by the National Cancer Institute of the National Institute of Health, Innovative Molecular Analysis Technologies (IMAT) Program under grant number R21CA206953, the BEST-IGERT program funded by the National Science Foundation DGE-1144901, the American Cancer Society, and an Institutional Research Grant (IRG).

Lastly, I would also like to express my deepest lifelong appreciation towards friends and family; Zhi, Kairie, Wilfred, Yash, Phinix, Stephanie, Mariana, Jose, and Dionne, for helping me get this far and opening doors I would have never imagined possible.

ABSTRACT OF THE THESIS

Constructing a Fluorescence Lifetime Nanoprobe Library to Advance Lifetime-Based Multiplexing

By

Louis Mejia

Master of Science in Biomedical Engineering

University of California, Irvine, 2019

Assistant Professor Jered B. Haun, Chair

Despite progress of the modern biomedical revolution, efficient personalized cancer cures remain largely elusive due to the vast amount of potential biomarkers to identify. This diverse pool of receptors is a product of a complex ecosystem of distinct key cell types within a tumor which may help promote proliferation. This intra-tumor heterogeneity has necessitated development of methods to identify key cell type receptors, such as molecular probes that target biomarkers. Probes harboring fluorescent species are among the most successful and couple distinct-spectra fluorescent species to a targeting protein, such as an antibody. However, existing probe libraries are limited to only 10 simultaneous detection channels, severely reducing the amount of ascertainable molecular information. Fluorescence lifetime imaging microscopy (FLIM) has been proposed as an expansion to conventional fluorescence imaging by adding an additional dimension of channels to analyze, but has been limited by the complexities of curve fitting decay half-lives. Recently, the phasor approach to FLIM provided an elegant means to analyze species mixtures on a phasor plot. Here, we demonstrate the construction of a lifetime probe library encapsulating a controlled

loading ratio of fluorescent species and analyzed with the phasor approach to FLIM. Using a reverse microemulsion synthesis method, organic dyes, dark quenchers, and quantum dots have been incorporated into probe cores to unlock a variety of distinct phasor positions within a single spectral window. Probe surfaces may be modified with polyethylene glycol chains to help prevent in-vitro protein adsorption and a functional loss of targeting specificity. Bioorthogonal click chemistry linkers may be conjugated onto chain termini to allow highly specific coupling to analogous premodified antibodies via rapid in-vitro two-step targeting of tumor biomarkers, or through the formation of immunoconjugates for direct targeting. Subsequently, the presence of key receptors may be inferred using the phasor approach. With the success of our preliminary probes, multiplexed targeting assays will follow. Ultimately, we intend to use our lifetime probe library in clinical settings to efficiently characterize tumors via simultaneous detection of up to 80 pre-selected personalized biomarkers.

Chapter 1

Introduction

At the present time, cancer remains the second leading cause of death in the United States [57]. This is due to the complex and dynamic heterogeneous microenvironment of tumors, hosting cell types known to indirectly promote proliferation [4]. Therefore, a molecular platform which can rapidly identify a vast array of key cell type biomarkers is necessary to help develop successful personalized treatments. To avoid the destruction of samples via popular statistically-driven massive-scale techniques, highly successful fluorescent exogenous probes have been developed for research in the past decades. Fluorescence lifetime imaging microscopy has been proposed an expansion to conventional fluorescence spectral imaging, but has been largely hindered by the inherent complexities of curve fitting decay half-lives. Recently, the phasor approach to FLIM was pioneered as an elegant way to resolve distinct lifetime species within the same spectral window by mapping data onto a semicricle phasor plot [12]. However, the phasor approach has not yet reached its full potential due to the lack of an existing library of probes utilizing this method.

In this project, we introduce the development of a fluorescence lifetime library of nanoprobes encapsulating various fluorescent species at controlled loading ratios. We propose the use of silica as a nanomaterial due its inherent biocompatibility and ease of surface modification [50, 37, 39]. Furthermore, due to homo-quenching and hetero-quenching energy transfer between adjacent fluorescent molecules, specific ratios of species can unlock distinct phasor plot positions to produce a wide array of potential probes for a lifetime library. Functional groups on silane molecules may be subsequently added onto probe exteriors as a basis for further modifications to act as a protective filler corona to shield probes from the biological environment [9]. Such modifications could help promote aqueous dissolution and prevent protein adsorption in targeting applications. Finally, bioorthogonal linker molecules could be conjugated onto the exteriors of protective corona coatings, intended to couple to corresponding molecules modified onto antibodies with high specificity in biological settings [43].

A three-part system of functionalized fluorescent probes, modified antibodies, and tumor cell lines harboring biomarkers of interest are intended to effectively couple during final targeting experiments. Ultimately, probes and antibodies are intended to form immunoconjugates prior to targeting in order to commence multiplexing assays with various optimized probes within a single spectral window. Thereafter, we intend to expand to multiple spectral windows with our library and allow simultaneous detection of several dozen biomarkers. Our final intention is to use our lifetime library of probes in clinical settings to characterize and elucidate useful information from a specific tumor samples in order to help develop successful personalized treatments.

Chapter 2

Background

2.1 Tumor Heterogeneity

While the rapid advancement of medical technology has given way to the full eradication of many diseases, such levels of containment for cancer have remained largely elusive. In 2018, cancer was ranked as the second leading cause of death in the United States at 1.7 million new cases and over 600 thousand fatalities [57]. While successful detection of superficial cancer types, such as skin and breast cancers, have shown remarkable survivability since the early 1990s peak death rate, other types, such as pancreatic and lung, remain difficult to detect or characterize at early onset.

Optical techniques, present since the 17th century, have allowed the preparation of histological stains and molecular detection probes to ascertain structure and function of diseased tissue. However, the vast knowledge gained from molecular biology during the modern era has necessitated far more molecular-level visualization, as it is

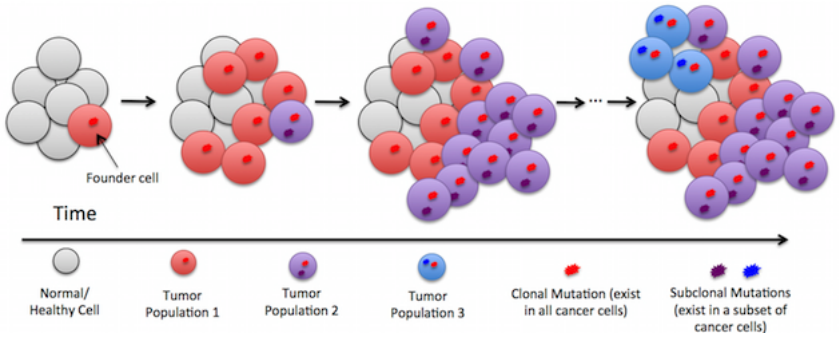

Figure 2.1: Normal cells progressively gain random malignant mutations, allowing the onset of heterogeneous tumors and potential for metastasis [54].

presently well understood tumors are highly variable, even within the same patient. This tumor microenvironment heterogeneity arises from immortalized neoplastic subpopulations, allowed to diversify via oncogene and tumor suppressor gene mutations, and from complex interactions between malignant cells and their neighboring cell ecosystem to help promote proliferation, drug resistance, and drug resistance [4, 25].

Key cell types include cells derived from hierarchical differentiation of cancer stem cells (CSCs), a rare population compromising less than 0.1% of tumor cells [51]. CSCs show substantially different therapeutic sensitivities compared to more differentiated cancer cells. It therefore remains undetermined which chemotherapeutic or radiotherapeutic agents effectively respond to this type. Endothelial cells, which may promote nutrient delivery to growing tumors via abnormal angiogenesis, are also of interest [40]. Inflammatory immune cells, such as myeloid suppressor cells (MDSC), regulatory T cells (CD4 and CD8), and tumor-infiltrating macrophages (M1 or M2 phenotype), may also be classified as a key cell type [8]. Densities of cytotoxic and memory T cells (CD3+, CD8+, and CD45RO+) are also of interest due to their potential as a prognostic metric [48]. Additionally, the identification of key tumor associated antigens, such as prostate cancer via PAP, PSA, and PSMA, have resulted

in remarkable therapeutic turnarounds in recent decades [36]. Thus, there is an outstanding need to rapidly elucidate large amounts of molecular information, which includes the identification of key cell types, within a specific tumor microenvironment to develop successful personalized treatments.

2.2 Molecular Diagnostics

Various molecular-level techniques have been implemented to help uncover more diagnostic data. This includes the current trend towards massive-scale omics, such as genomics, proteomics, glycomics, lipidomics, and metabolomics. Methods in these fields, such as mass spectrometry and next generation sequencing, operate via destruction of a large heterogeneous sample, which is then analyzed at bulk, revealing population averages of harvested molecules of interest [55]. However, large scale analysis results in loss of structural information and molecular expression levels. Furthermore, uncommon sub-populations of markers or cells become exceedingly difficult to identify, such as rare CSCs. Single-cell transcriptional analysis technologies attempt to circumvent the exclusion of statistical outliers within a population at large [31]. Nonetheless, spatial information within individual cells is still lost, including the ability to predict signaling pathways, epigenetic regulation, and non-genetic variance [38, 24, 49, 23]. As such, molecular probes are the only remaining solution to retain spatial or molecular expression information with cellular-level resolution.

Numerous varieties of molecular targeting probes presently exist, of which the most successful and widespread is fluorescence-based imaging. These fluorescence-based probes, using different excitation and emission spectra, are only limited by the com-

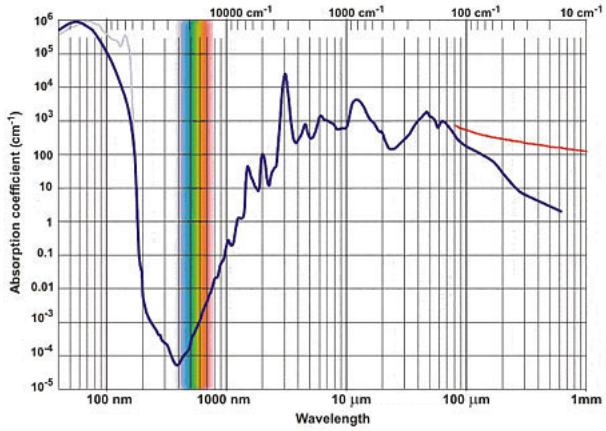

Figure 2.2: The absorption spectrum of water limits biological applications of fluorescent probes to wavelengths between 200 and 2000 nm wavelength [13].

bination of appropriate filter sets and total number of non-overlapping spectra given by probes. A wide array of visible and near-infrared probes are presently available, typically allowing for 5-10 detection channels [20]. Probes outside this region are generally avoided due to strong water absorbance obstructing biological use [56]. Ultraviolet probes pose an additional tissue hazards, while far infrared probes tend to overlap with the 10 µm thermal radiation peak of human bodies.

Other alternative molecular probes use non-fluorescent modalities for detection channels, such as surface-enhanced Raman scattering (SERS) and mass spectrometry. SERS utilizes the coupling of plasmonic nanoparticles with reporter molecules, which produce unique oscillations of free electrons, or fingerprints, via Raman scattering [47]. While up to 30 channels have been estimated due to the narrow width of Raman bands, in practice the complexity of spectral unmixing and the possibility of localized heating with more probes limits SERS to approximately 10 targets [58]. Mass cytometry, in turn, utilizes rare earth metal isotope tags on samples for mass spectrometry, demonstrating the potential of up to 32 channels via cell or tissue image scans [2]. However, over three hours are required to scan targets at 1 µm resolution,

comparably lower than optical techniques. While, multiplexed ion beam imaging (MIBI) has demonstrated up to 10 channels at sub-micron resolution in breast tumor samples, 2 scans require an hour to complete [1]. Aside from long scan durations, mass spectrometry systems also require the destruction of a sample, preventing any further analyses, and are often quite complex and expensive. Thus, there is a need to develop a molecular diagnostic platform with similar simplicity, speed, and specificity as spectral fluorescence imaging.

2.3 Fluorescence Lifetime Imaging Microscopy

An exciting expansion to conventional fluorescence imaging incorporates the use of fluorescence lifetime imaging microscopy (FLIM) as a second dimension of detection channels. Fluorescence lifetime is defined as the intrinsic duration a fluorescent species remains in its excited state before emitting a photon, determined from both radiative and non-radiative processes as energy dissipates from the molecule to the ground state [30]. While organic fluorophores generally retain lifetimes between 0.5 - 4 nanoseconds (ns), other fluorescent species, such as long-lifetime dyes or semiconductor nanoparticles (quantum dots) may exhibit lifetimes in the range of 10 - 100 ns. FLIM is of interest since multiple species can share the same overlapping spectra but exhibit distinct fluorescence lifetimes.

2.3.1 Curve Fitting Decay Half-Lives

Conventionally, lifetime is quantified by curve fitting a decay half-life for a population [20]. Using a short excitation pulse, an intrinsic decay composed of N fluorescent

species can be modeled by Eqn. (2.1).

$$\hat{I}(t) = \hat{I}(0) \sum_{i=1}^{N} \alpha_i e^{-t/\tau_i} \tag{2.1}$$

$\hat{I}(0)$ is the number of instantly emitted photons at time zero, α_i is the amplitude, and τ_i is the fluorescence decay time of the i-th species [7, 17]. The amplitude-weighted lifetime, τ_a (or the apparent lifetime), is typically used to determine energy transfer efficiency. The average lifetime $\langle\tau\rangle$ contains f, the fractional contribution of the i-th species to the total intensity.

$$\tau_a = \sum_{i=1}^{N} \alpha_i \tau_i \qquad \langle\tau\rangle = \sum_{i=1}^{N} f_i \tau_i \qquad f_i = (\alpha_i \tau)/\tau_a \tag{2.2}$$

Finally, the measured decay $I(t)$ is simply a convolution of the intrinsic decay and the instrument response function (IRF) plus any background noise in the system $n(t)$ shown in Eqn. (2.3).

$$I(t) = IRF \otimes \hat{I}(t) + n(t) = IRF \otimes \left\{ \hat{I}(0) \sum_{i=1}^{N} \alpha_i e^{-t/\tau_i} \right\} + n(t) \tag{2.3}$$

FLIM can be conducted in either the time or frequency domains, which involves measurements of scattered excited light or the use of a fluorescence lifetime standard of known lifetime to calibrate the IRF in one-photon excitation, respectively.

Most FLIM analysis methods curve fit measured data, often via an iteratively constrained optimization algorithm to estimate parameters α and τ [44, 16]. Each iteration compares parameters to measured data, which provides feedback for further optimizing the model. Non-linear least squares estimation is the current analysis method of choice for both time and frequency domains. First, a simple decay model,

usually a single exponential decay, is used to make initial guesses to parameters. Normally, a chi-square value is used to examine the computer algorithm fit, and if rejected, a more complicated decay model is used, typically adding another exponent. Often, this process is quite complex, largely due to low photon counts in real systems. As such, no universal method has been established to accept or reject models and an expertise level of physics is required, in which the validity of the statistical tools are debatable. Presently, no more than 3 exogenous probes have been resolved using curve fitting of decay half-lives.

2.3.2 The Phasor Approach

The phasor approach to FLIM, pioneered by Gratton et al. in 2008, offers an elegant solution to alleviate the issues with curve fitting decay half-lives by transferring data into the frequency domain and graphing onto a polar plot [12, 45]. A decay trace $I(t)$ is measured at each pixel location and subsequently plotted as a phasor, drawn as a semicircle curve centered at (G = 0.5, S = 0.5) with radius 0.5, by applying sine and cosine transforms equivalent to the real and imaginary components of a Fourier transform shown in Eqns. (2.4).

$$g(\omega) = \frac{\int_0^\infty I(t)cos(\omega t)}{\int_0^\infty I(t)} \qquad s(\omega) = \frac{\int_0^\infty I(t)sin(\omega t)}{\int_0^\infty I(t)} \tag{2.4}$$

After calibration of the phasor plot to a known decay trace, by solving integrals for Eqns. (2.4), the following equations are produced to give a direct relationship between a set of phasor positions and their corresponding lifetimes.

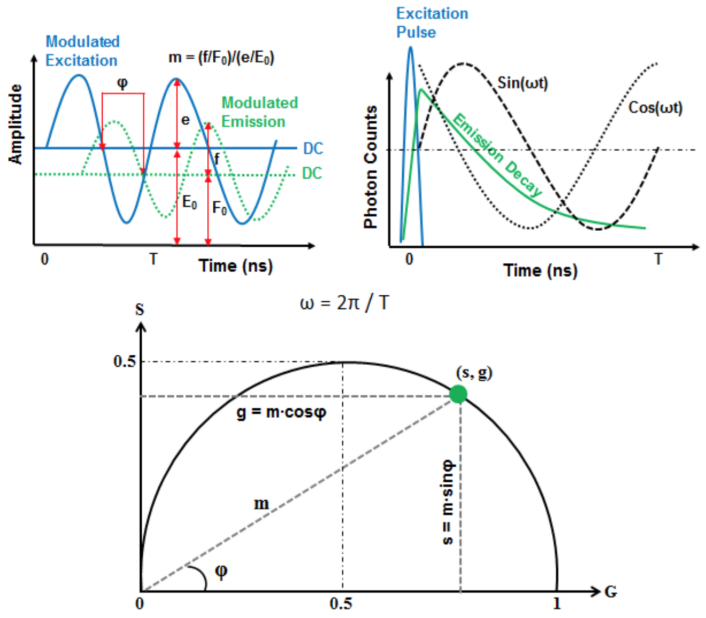

Figure 2.3: Mapping frequency and time domain FLIM data on the phasor plot [32].

$$g = \sum_{i=1}^{N} \frac{f_i}{1+\omega^2\tau_i^2} \qquad s = \sum_{i=1}^{N} \frac{f_i\omega\tau_i}{1+\omega^2\tau_i^2} \tag{2.5}$$

In the condition of a single-lifetime fluorescent species, these equations reduce to follow direction relationships shown in Eqns. (2.6). While single-lifetime species are plotted directly onto the semicircle arc, complex multiple-lifetime species are decomposed as a linear combination of multiple phasors, and appear within the semicircle.

$$g = \frac{1}{1+\omega^2\tau^2} \qquad s = \frac{\omega\tau}{1+\omega^2\tau^2} \qquad \tau = \frac{1}{\omega}\left(\frac{s}{g}\right) \tag{2.6}$$

The power of the phasor approach stems from its ability to act as a quantitative ruler measuring both single-lifetime and complex lifetime species. The plot can also be shifted to center on a specific lifetime foci by using different modulation frequencies (i.e at 80 MHz the top of the semicircle lies at 2 ns, or 8 ns for 20 MHz). Positions to

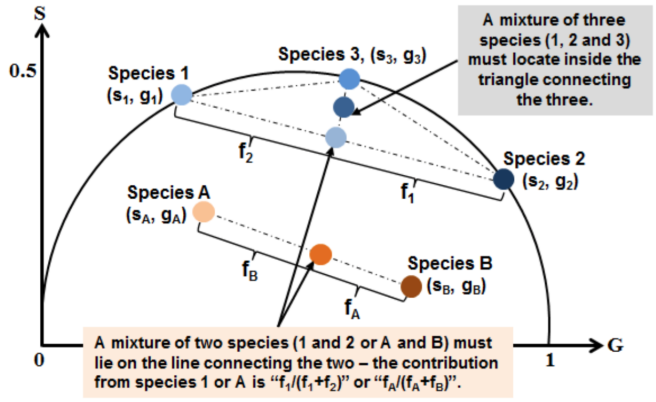

Figure 2.4: Linear unmixing of multiple fluorescent species on the phasor plot [32].

the far right approach a lifetime of zero, while those to the far left approach an infinite lifetime. In mixtures, the distance between two component species is proportional to the fractional contribution of each species, allowing for quantitative analyses of constituents. Three or more species will produce a theoretical polygon in which the signal mixture may appear (Fig. 2.4).

2.3.3 FLIM Phasor Applications

The phasor approach to FLIM can also qualitatively analyze fluorescence quenching in systems, including Förster resonance energy transfer (FRET), Dexter electron transfer, and dark quenching. FRET is defined as non-radiative energy transfer between an excited molecule and donor molecule via dipole-dipole interactions at distances less than 10 nm, and has been extensively studied with the phasor approach for the past decade [14, 28].

Short-distance quenching effects between two fluorescent species of the same kind (homo-quenching) or different kind (hetero-quenching) in a donor-acceptor pair in-

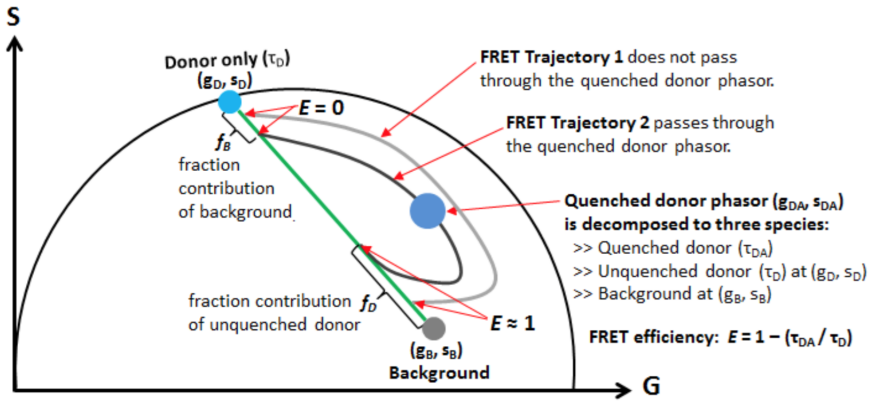

Figure 2.5: Analyses of FRET trajectories with the phasor plot [32].

teraction are of particular interest. Either two fluorescent species can be used together as a donor-acceptor pair, or a dark quenching dye can act as an acceptor. Unlike a fluorescent acceptor, a dark quencher absorbs energy and emits it as heat [6]. Any significant quenching effect produced by an acceptor molecule will also change the lifetime of the donor-acceptor pair compared to a donor-only sample. This effect can also be visually seen on the phasor plot (Fig. 2.5). Coupling of quantum dots and quenchers have been further shown to accelerate lifetime, highly dependent on dose.

Since the advent of the phasor approach to FLIM, over 10 cellular autofluorescent species have been identified in distinct locations on the phasor plot [52]. This approach has also seen success in studying cellular metabolism, the endomembrane system, and cancer malignancy [15, 29, 41]. Nonetheless, the full potential of the phasor approach has not yet been realized, as no exogenous probes have been developed incorporating the extra dimension of FLIM to couple with conventional fluorescence spectral imaging due to the limitations of curve fitting decay half-lives.

The phasor approach provides the potential to create the first fully functional lifetime probe library. Such a lifetime library would need to be developed from a wide array

of fluorescent species encompassing both the full range of wavelengths used in fluorescence spectral imaging (such as the Alexa Fluor series) and a large range of different fluorescence lifetimes for each spectral window (0.5 - 50 ns). Using 8 different spectral detection channels, each with 10 distinct-lifetime fluorescent species, up to 80 unique probes and detection channels may be created. This project will demonstrate the construction of a lifetime probe library using fluorescent nanomaterials encapsulated within silica, each distinctly resolved using the phasor approach to FLIM, within the context of tumor characterization via biomarker targeting.

Chapter 3

Synthesis

To begin construction of our library of probes, we first sought to produce a probe core encapsulating mixtures of fluorescent species at specific loading ratios. Numerous nanomaterials have been used to transport reporter molecules or therapeutic agents in a wide array of medical applications, with varying degrees of success, such as iron oxide crystals, gold nanorods, and polymer liposomes or micelles [22]. For our probe cores, amorphous silica was selected due to existing simple synthesis protocols, low toxicity, unhindered fluorescence of encapsulated species, and feasibility for easy surface modifications via triethoxy silane molecules [37, 39].

3.1 Reverse Microemulsions

The sol-gel process, commonly used by material scientists, incorporates small precursor molecules to form a larger object, often in the form of polymerous gels [10]. In 1968, Werner Stöber first pioneered the highly popular adaptation of this process to

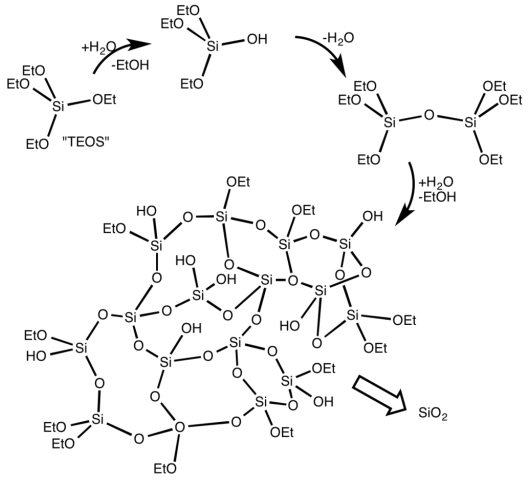

Figure 3.1: Hydrolysis and condensation of TEOS in the Stöber Process.

synthesize silica nanoparticles, now known as the Stöber process [50]. The precursor molecule, tetraethylorthosilicate (TEOS), is hydrolyzed with water, in the presence of ammonia as a catalyst, and allowed to form larger structures via condensation with other TEOS molecules (Fig. 3.1). Variations of the Stöber process have been able to produce solid core probes, shell-core probes, hollow shells, mesoporous probes, and other nanomaterials.

$$Si(OEt)_4 + H_2O \rightarrow Si(OEt)_3OH + EtOH$$

$$2Si(OEt)_3OH \rightarrow (EtO)_3Si\text{-}O\text{-}Si(OEt)_3 + H_2O$$

The Haun group previously experimented with different renditions of this process, and ultimately selected synthesis of silica via reverse microemulsions [34]. This adaption has been optimized to use 1.3 mL of IGEPAL-CO520 surfactant to produce water-in-oil drops within 10 mL of cyclohexane. Organic fluorescent dyes, dark quencher dyes, or hydrophobic quantum dots of interest are subsequently added. 150 μL ammonium hydroxide (30% in water) is added to form droplet interiors. Finally, 80 μL of TEOS is

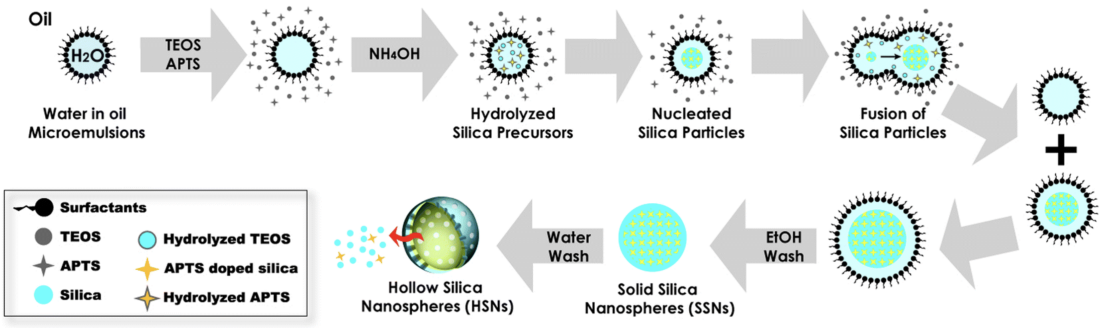

Figure 3.2: Mixtures of triethoxy silane and TEOS will form hollow or porous silica in reverse microemulsions. Presence of only TEOS forms solid silica cores [33].

added and allowed to react for 24 hours to produce silica particle cores (see Appendix A.1 for protocol). Gradually, fluorescent species are shuttled into the drop interior and embedded within a silica mesh.

In order for either organic fluorescent dyes or dark quencher dyes to successfully incorporate into the particle interior, both must be purchased or premodified with an N-Hydroxysuccinimide (NHS) leaving group. These dyes, stored in dimethylformamide (DMF), are then reacted with (3-aminopropyl)triethoxy silane (APTS) for 24 hours in ethanol (Fig. 3.3). APTS, a triethoxy silane, retains a structure similar to TEOS, with one of four ethoxy chains replaced by a propyl chain terminating in a primary amine. The remaining three ethoxy chains can be used to react with TEOS for incorporation into the silica probe.

Fluorescent semiconductor nanoparticles, known as quantum dots, are particularly exciting for exhibiting broad absorption bands, narrow emission peaks, size-tunable emission spectra, and long fluorescence lifetimes. Large quantum dots premodified with hydrophobic surface ligands can be directly added to the synthesis reaction without any additional modifications, due to a TEOS transfer mechanism which shuttles hydrophobic quantum dots into the hydrophilic drop interior [27].

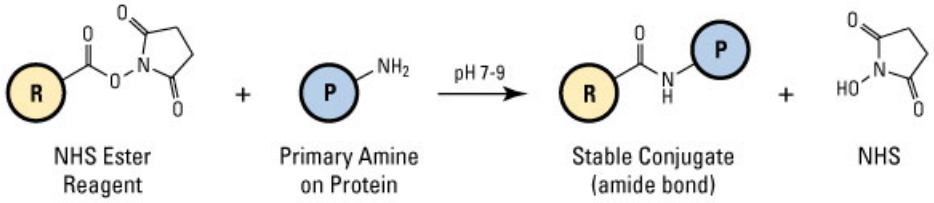

Figure 3.3: Dyes labeled with NHS leaving groups will form amide bonds with primary amine reagents, specifically a triethoxy silane [19].

To help populate numerous different positions on the phasor plot of a single emission window (initially yellow-orange), two additional projects in the Haun Group incorporate an exploratory array of quantum dots and fluorescent dyes, respectively, from various vendors. Fluorescent dyes tested include Alexa Fluor 555, BODIPY TMR-X, and Rhodamine from Thermo Fisher, and KU530 from KU Dyes. Quantum dots from Invitrogen, NN-Labs, Ocean NanoTech, and Strem have also been tested, which include both spheres and rods, and cores made from cadmium selenide, copper indium sulfide, indium phosphide, and manganese-doped zinc sulfide. Additionally, mixtures of fluorescent dyes or quantum dots and dark quenchers, namely QXL 570 and QXL 610 from Anaspec, have been tested. The remainder of this project uses silica probes encapsulating quantum dots as a basis for testing further modifications.

3.2 Surface Silanization

Much like APTS, other triethoxy silane molecules may be added after 24 hours of core synthesis to functionalize surfaces for further modifications. To remove unreacted material and allow the transfer of probes into aqueous solution, particles are washed via four rounds of centrifugation to produce a pellet, supernatant disposal, and pellet resuspension, via ethanol as an intermediate solvent.

Once washed, particles may be either directly analyzed or undergo further modification via covalent addition of molecules to surface functional groups. Our typical analyses use dynamic light scattering (DLS) to determine probe size via a Malvern Zetasizer Nano DLS system, absorption spectroscopy with a Cary-60 instrument, fluorometry with a Cary Eclipse instrument, scanning electron microscopy (SEM) with a FEI Magellan 400 XHR system, transmission electron microscopy (TEM) with via a FEI-Philips CM20, or the phasor approach using a custom-built FLIM system and software (SimFCS) developed by the Laboratory for Fluorescence Dynamics at the University of California, Irvine.

An example of SEM, phasor, yield, and DLS results of quantum dots within silica probes are shown in figure 3.4. Increasing volumes of QXL dark quencher dyes were loaded into probe cores to unlock distinct phasor positions, shown in (C). Of particular note, additional modifications to particle surfaces have no effect on phasor plot position. Unless specifically stated, the remainder of this project will display results of silica probes incorporating CZ quantum dots with core-shell architecture, cadmium selenide and zinc sulfide respectively, from NN-Labs. These quantum dots were specifically chosen for retaining a bright 590 nm emission peak, low price, high concentration, and hydrophobic octadecylamine stabilizing surface ligands.

Along with determining the appropriate silica probe architecture for co-encapsulating mixtures of fluorescent species, work previously done in the Haun Group determined the appropriate reagent quantities during core probe synthesis, but left particles either with no surface silanization (terminating in ethoxy chains) or modified with APTS. Both a lack of surface silanization and the addition of APTS were unable to disperse probes in water or PBS, and produced large aggregates.

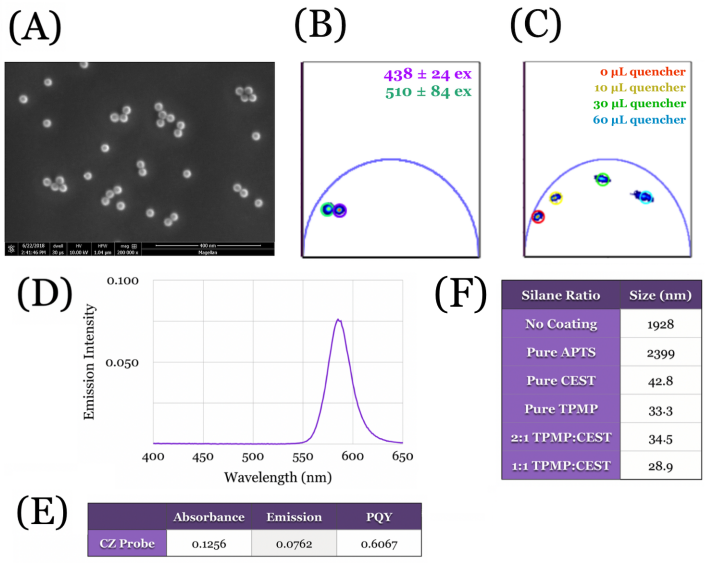

Silane Ratio	Size (nm)
No Coating	1928
Pure APTS	2399
Pure CEST	42.8
Pure TPMP	33.3
2:1 TPMP:CEST	34.5
1:1 TPMP:CEST	28.9

	Absorbance	Emission	PQY
CZ Probe	0.1256	0.0762	0.6067

Figure 3.4: CZ Probes analyzed with (A) SEM, (B) phasor approach at two different excitations, (C) phasor approach with increasing amounts of quencher, and (D-E) fluorometry and absorbance spectroscopy to calculate PQY. (F) DLS results of different surface silane ratios.

To help alleviate probe aggregation, carboxyethylsilanetriol (CEST) from Gelest and 3-(trihydroxysilyl)propyl methylphosphonate (TPMP) from Sigma Aldrich were added to particle surfaces at different molar ratios. Carboxylic acid was specifically chosen as the base for future modifications via carbodiimide crosslinking (full details in section 4.1), while phosphonate groups should help prevent aggregate formation and render efficient aqueous dissolution. The effectiveness of aqueous dissolution necessitated the use of filtered centrifuge tubes for washing all further modifications discussed in chapter 4 instead of pelleting particles via the typical post-synthesis wash protocol. With these functional groups, probe cores were able to produce consistent DLS results of 40 nm. A 1:1 molar ratio of CEST:TPMP was selected as most viable, and is used for the remainder of this project.

The density of silicon atoms on the surface of each synthesized probe, at an estimated

1:1 ratio of quantum dots to silica probes, was used as the basis for further estimates [21]. Assuming an excess of surface silanes, an estimated 33,000 functional groups were present on probe surfaces, of which 17,500 were carboxylic acid moieties (see Appendix B.2 for calculation). Initially, 30 μL of total silane was arbitrarily added to surfaces (20 μL CEST, 10 μL TPMP). However, these calculations also determined a 60-fold excess of surface silane was added to reactions, and was later suspected as hindering early modifications (see section 3.3).

To illustrate this, an assay of probes was prepared using different amounts of total surface silane while still retaining a 1:1 CEST:TPMP molar ratio (DLS results shown below). Select samples were imaged under SEM which revealed a large 300 μL excess of total surface silane created smooth-surface 200 nm structures. Surprisingly, the high energy electron beam decomposed these structures over the course of several minutes (Fig. 3.5), allowing silica probes trapped in excess silane to become visibly discernible. Ultimately, it was determined a large excess was detrimental for synthesis. The remainder of this project uses particles modified with a total of 3 μL of surface silane (2 μL CEST, 1 μL TPMP).

3.3 Encapsulation Optimization

Initially, Qdot 585 ITKs, bright core-shell organic quantum dots (CdSe/ZnS) from Invitrogen, were used for early syntheses and modifications. However, calculations used to determine the total number of silica probes in a standard synthesis revealed there should more probes than quantum dots, by an order of magnitude (see Appendix B.1 for calculation). This illustrated the vast majority of our probes should be void of

(A)

Total Silane	Size (nm)
0 µL	67.8
1 µL	52.2
3 µL	44.1
10 µL	44.3
30 µL	45.7
100 µL	54.1
300 µL	207
1000 µL	224

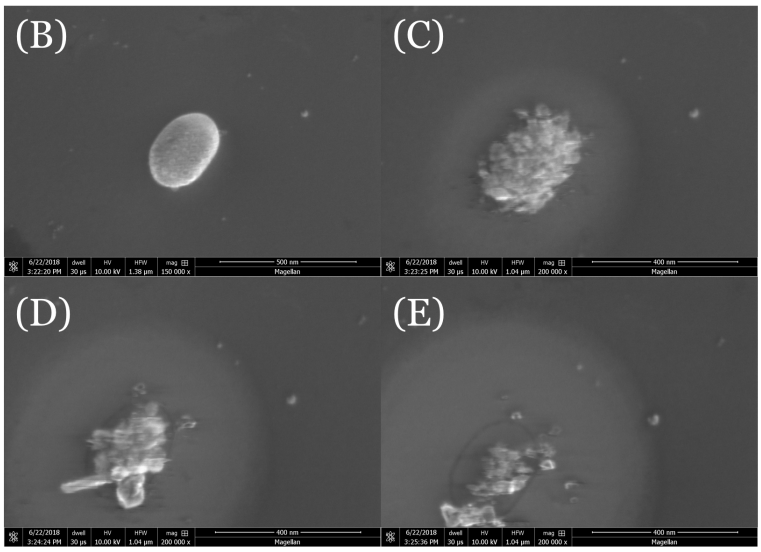

Figure 3.5: Variation of total surface silane at 1:1 CEST:TPMP molar ratio. Analyzed with (A) DLS. (B-E) SEM timelapse of 300 µL total silane taken 1 minute apart.

quantum dots and composed entirely of silica. To test this, silica probes encapsulating Invitrogen quantum dots were imaged using TEM (Fig. 3.6). As predicted, by loading 100 µL of quantum dots into the synthesis reaction only 10-15% of silica probes were found to have any discernible quantum dots.

To compensate for this, experiments were conducted to decrease the proportional ratios of all other reagents during a synthesis, allowing for a higher concentration of quantum dots (5x, 10x, and 20x more concentrated). However, both size results and TEM images revealed silica probes became substantially smaller, and irreversibly aggegrated together. We believe the proportionally larger amount of decane solution quantum dots are inherently in, disrupt the reverse microemulsion synthesis.

While a side project went on to explore alternative approaches to efficiently use Invitrogen quantum dots in probes, the primary quantum dot of focus was switched to the comparatively inexpensive and 5x more concentrated CZ particle from NN-Labs.

(A)

Invitrogen Conc.	Size (nm)
0x Increase	43.1
5x Increase	63.2
10x Increase	146
20x Increase	246

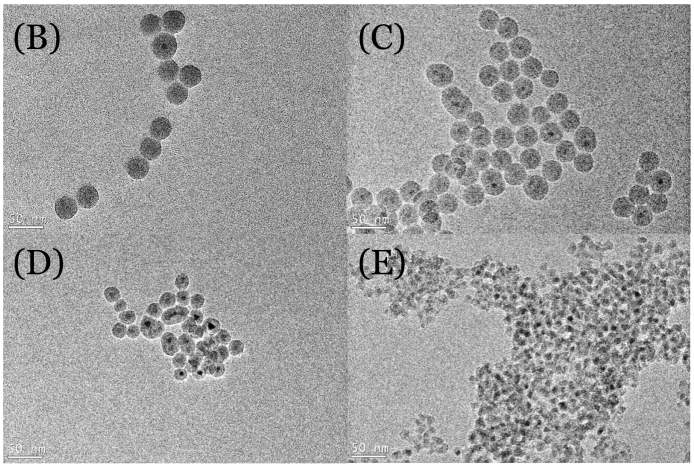

Figure 3.6: Concentration of 100 µL Invitrogen QDs via proportionally increasing all other synthesis reagents. Analyzed with (A) DLS and (B-E) TEM. Note the vast majority of silica probes have no visible QDs in (B).

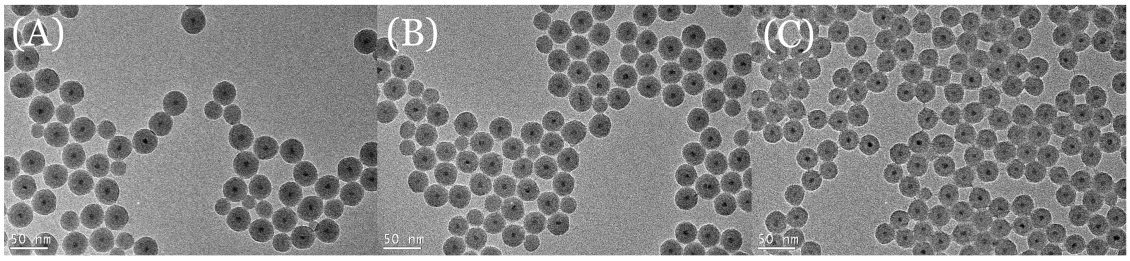

Figure 3.7: Determination of 1:1 QD:Probe ratio using CZ QDs at (A) 100 µL, (B) 150 µL, and (C) 200 µL.

An assay of different synthesis loading volumes was used to determine the appropriate 1:1 ratio of quantum dots to silica probes (Fig. 3.7), which visually estimated 200 µL of CZ particles would be enough to fill most probes. Note that some silica probes appear to be smaller and have no encapsulated quantum dots, while others appear to have multiple. For the remainder of this project, all modifications and targeting experiments employ 200 µL of CZ quantum dots from NN-Labs.

It should be noted that this metric is simply an estimate for standardizing later experiments. Furthermore, based on assays conducted with increasing amounts of

(A)

	Size (nm)
TEOS Stock	4371
6 Month Old	49.1 (88.7%) 5319 (11.3%)
2 Week Old	45.2 (97.9%) 4811 (2.1%)

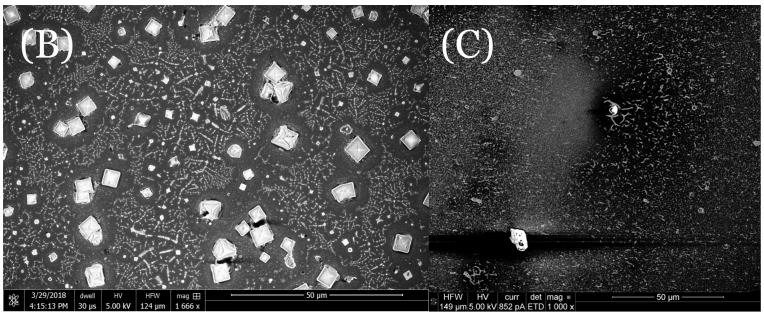

Figure 3.8: Detection of large crystal structures post-synthesis via (A) DLS and in SEM with a (B) 6 month and (C) 2 week old samples.

CZ quantum dots, the phasor position did not shift from homo-quenching effects, indicating subtle differences in our quantum dot loading volumes have no significant effect on phasor results. Molar concentrations given by NN-Labs indicate $6.0 * 10^{14}$ quantum dots should be present during core synthesis, and here, we assume for all future modifications and targeting that an equivalent amount of probes is produced, given the estimated 1:1 ratio.

Of particular interest, both DLS and SEM results (Fig. 3.8) occasionally indicate the presence of large crystalline structures, post-synthesis. These structures continue to appear in later modifications and targeting, indicating probes have either aggregated together during synthesis or crystals gradually formed within the TEOS stock solution. DLS results of the stock solution have alluded to the latter explanation. In either case, a significant amount of probes, and silica precursor, could be lost to these structures. Section 5.3 provides a solution for removal of these structures via size exclusion chromatography (SEC).

Recently, a NanoSight system from Malvern was installed at the University of California, Irvine. Future experiments will attempt to gain a higher precision of the total number of silica probes produced from reverse microemulsion synthesis.

Chapter 4

Modifications

Despite the high level of aqueous dissolution instilled by carboxylic acid and phosphonate surface moieties, timescales of several weeks to months have shown probes precipitate out of solution at concentrations of 90 nM. Furthermore, unmodified silica probes are known to adhere to glass surfaces, hindering cell targeting assays with conventional glass slides. Thus, direct conjugation of an antibody to probe will not result in successful targeting, and must first undergo modification with protective molecules. Short linkers could then be covalently reacted onto the ends of these molecules to act as a bridge to an antibody of interest.

4.1 Primary PEGylation

While protective molecules are used to encapsulate probe core for various purposes (such as biomarker targeting, blood transport, membrane fusion, etc), most probes must first successfully arrive at a location of interest, often in aqueous solution [53].

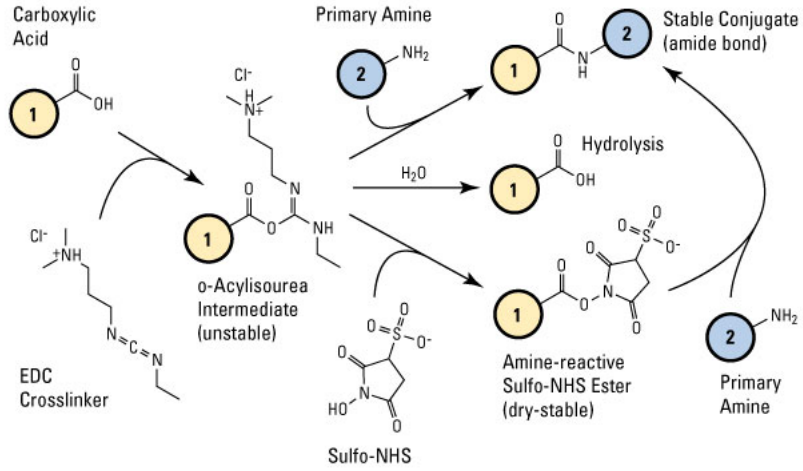

Figure 4.1: Carbodiimide EDC crosslinks amines and carboxylic acids to form an amide bond. Addition of NHS (bottom-most pathway) increases efficiency [19].

As a result, one of the most popular protective molecules is polyethylene glycol (PEG) due to its biocompatibility, immunocompatibility, and hydrophilic nature [5, 35].

Amine-terminating PEG chains may be conjugated onto carboxylic acid moieties via carbodiimide crosslinking using N-(3-Dimethylaminopropyl)-N-ethylcarbodiimide hydrochloride (EDC) and NHS (Fig. 4.1). In the presence of EDC crosslinker, carboxylic acid groups will temporarily form an o-Acylisourea intermediate group. However, this product is highly unstable and will rapidly hydrolyze and revert back into a carboxylic acid. NHS is instead added to help form a dry stable intermediate, replacing EDC, to become a favorable leaving group in the presence of a primary amine and form an amide bond.

To help drive the reaction, a molar excess of EDC and NHS was selected, in comparison to PEG. When reacted for 3 hours, favorable results have been produced with a 10x excess of EDC and a 3x excess of NHS, specifically chosen for the multiple reaction pathways EDC may take. While our own calculations had predicted 6.55

silane groups could be loaded onto a square nanometer on a silica probe, Dai et al. had previously determined approximately 6 PEG molecules may occupy a nm^2 on a probe surface [9]. Assuming a molar excess, the theoretical basis of 6 PEG chains per nm^2 was used to determine a 40 nm probe may have up to 30,000 PEG chains on its surface (see Appendix B.2 for calculation).

Synthesized probes in water were used as two-thirds of the total volume in PEG reactions. Stock solutions for EDC and NHS, purchased from Sigma Aldrich and stored dry, were diluted in water immediately before usage. Azido-PEG35-amine (AzPEG) and methoxy-PEG36-amine (mPEG36), purchased from BroadPharm and stored in DMF, were used for all PEG reactions at various ratios. Azide moieties were specifically selected for future linker attachments (detailed in section 4.3), while mPEGs act as nonreactive hydrophilic filler chains (see Appendix A.2 for protocol).

Long AzPEG and mPEG chains, 15 nm in size, allow a maximum addition of 30 nm to probe sizes if fully extended via brush configuration of the PEG corona. Thus, fully PEGylated probes should retain sizes of 60-70 nm (Fig. 4.3).

4.2 Backfill PEGylation

Research conducted by Dai et. al had previously determined low-density PEGylated probes used for in-vivo targeting have the tendency to adsorb smaller proteins between PEG chains. [9]. As part of the innate immune system, these proteins subsequently recruit larger proteins to engulf probes via formation of a large protein corona, ultimately rendering probes as ineffective targeting agents. Simply increasing the density of PEG molecules will prevent the adsorption of proteins, however, surface crowding

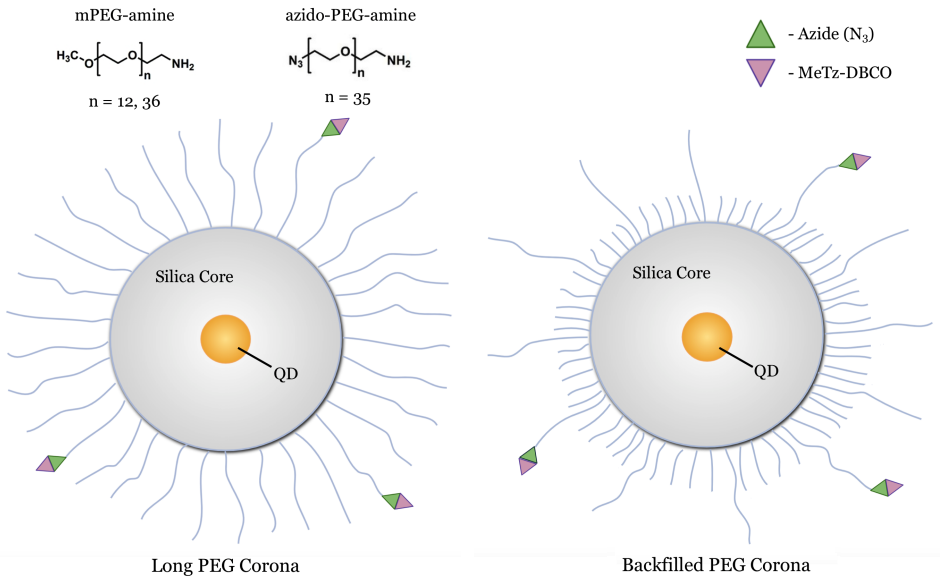

Figure 4.2: Probes undergo either primary PEGylation with long Az-PEG35-amine and mPEG36-amine chains, or additional backfill PEGylation with short mPEG12-amine chains. MeTz-DBCO linkers are added as a final modification at azide moieties.

will also hinder the binding efficiency of specific functional groups on the termini of PEG chains.

To circumvent these issues, a second "backfill" PEGylation reaction can be performed on probes, using much smaller and more numerous filler chains. We were particularly interested if the reported effects of backfilled PEG chains would produce favorable binding to cell surfaces and prevent particle adsorption to glass surfaces.

Specifically, we opted for mPEG12-amine, purchased from BroadPharm, for backfill modifications. 90% of PEG chains added were shorter mPEG12 chains, while the remaining 10% were one of a select ratio of mPEG36 and AzPEG. Backfilled probes underwent a second 3 hour PEGylation reaction, still retaining a 10x molar excess of EDC and 3x excess of NHS.

Of note, higher densities of mPEG on a surface appear to force the PEG corona

(A) mPEG36 Only

mPEG36 Added	Size (nm)
0 mmol	33.9
0.1 mmol	39.6
0.3 mmol	39.8
1.0 mmol	42.1
3.0 mmol	60.6

(B) AzPEG35 & mPEG36

AzPEG %	Size (nm)
0% Az	38.5
0.3% Az	37.2
1.0% Az	43.0
3% Az	45.1

(C) Backfill (Az & mPEG36)

AzPEG %	Size (nm)
0% Az BP	65.3
0.3% Az BP	65.1
1.0% Az BP	57.4
3% Az BP	53.8

(D) MeTz (Az & mPEG36)

AzPEG %	Size (nm)
0.3 % Az	32.1
1.0% Az	33.1
3.0% Az	40.9
0.3% Az BP	52.1
1.0% Az BP	43.3
3.0% Az BP	43.8

Figure 4.3: DLS results at different loading ratios of (A) long mPEG36 chains, (B) AzPEG and mPEG36, (C) AzPEG and mPEG36 with 9:1 mixture of backfilled mPEG12 to total PEG, and (D) MeTz-DBCO added at a 3x molar excess.

into an extended brush configuration. However, higher densities of AzPEG appear to decrease the size of the corona. This effect might be due to the greater hydrophobic nature of azide moieties.

4.3 Click Chemistry Linkers

Before probes can be bound to antibodies, appropriate pairs of linkers must be added to probe exteriors and antibodies. While creation of immunoconjugates (ICs) prior to targeting is the ultimate intention of our probe system, the process of creating ICs require an additional series of steps including size exclusion chromatography (SEC) featured in section 5.3. To facilitate this process, a two-step targeting approach was initially selected for proof of concept. This method first allows modified antibodies to react to biomarkers of interest on tumor cells, and is followed by the addition of fully functionalized silica probes.

To employ the successful use of two-step targeting within a biological system, reactive moieties between probes and modified antibodies must be highly specific to one another with minimal side reactions. As such, bioorthogonal reactions, which use

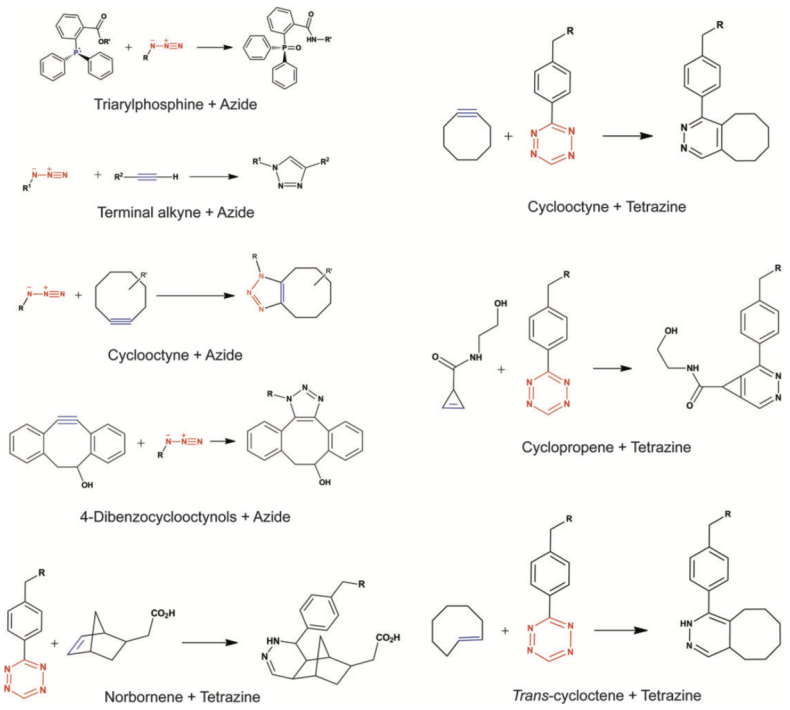

Figure 4.4: Popular bioorthogonal reactions using Diels-Alder mechanisms [43].

chemistry not conventionally found within biological systems, are of interest. A wide array of click chemistry linkers have been extensively studied for these purposes over the last two decades. Ideally, reactions between linkers should also occur rapidly in biological conditions (i.e pH and temperature), limiting the production of toxic and non-toxic byproducts [43]. The table below details a list of popular bioorthogonal reaction schemes.

Of particular note is the extremely fast reaction rate of trans-cyclooctene (TCO) and tetrazine, which employs an inverse-electron-demand Diels-Alder cycloaddition and has allowed for its extensive use in live cell imaging in-vitro and in-vivo [11, 46]. However, the instability of tetrazine over prolonged time scales necessitates use of its more stable methyltetrazine (MeTz) analog in our primary two-step coupling, characterized by a reaction rate constant of 880 M^{-1} s^{-1} [26]. For our primary probe

Reaction	Reaction scheme	Rate constant (M^{-1} s^{-1})	Comments
Staudinger ligation	Triarylphosphine+azide	10^{-3}	- Slow reaction speed - Phosphine oxidation
CuAAC	Alkyne+azide	Up to 10^{4}	+ Fast reaction speed + Simple reactants - Cytotoxic - Reduces protein and quantum dot fluorescence - Potential negative effects of acidic reaction conditions (iron oxide)
Cyclooctyne-based, strain-promoted cycloaddition	Cyclooctyne+azide	10^{-3}	+ No catalyst required
	Fluorinated cyclooctyne+azide	10^{-3}–10^{-1}	- Slow reaction speeds
	4-Dibenzocyclooctynol+azide	2	- Difficult synthesis of cyclooctyne and derivatives
	BARAC+azide	1	- Poor solubility of dienephiles
Tz-based, inverse-electron-demand Diels-Alder Cycloaddition	Norbornene+Tz	1	+ Extremely fast reaction speed (TCO)
	Cyclooctyne+Tz	10	+ Can tailor reaction speed or application need with range of dienephiles
	Cyclopropene+Tz	10	+ Can tailor reaction speed with a range of Tzs
	Trans-cyclooctene+Tz	10^{4}	- Poor solubility of dienephiles

Figure 4.5: Popular bioorthogonal reactions with corresponding reaction rates and additional comments [43].

to antibody reaction, we terminated silica probes with MeTz and modified antibodies with TCO (detailed in section 5.1).

Before the primary MeTz to TCO coupling could commence, MeTz moieties need first undergo conjugation onto probe termini. Specifically, this required modification of azido groups on AzPEG chains with a small molecule carrying MeTz. 4-Dibenzocyclooctynol (DBCO) was chosen as the appropriate molecule to couple with the azido group via the slower Az-DBCO reaction. MeTz-DBCO, purchased from Click Chemistry Tools (shown below), was allowed to react for 24 hours with Az-probes in the presence of DMF and subsequently washed using filtered centrifugation tubes (see Appendix A.3 for protocol). A 3x molar excess of MeTz to AzPEG chains per silica probe was used for all remaining studies.

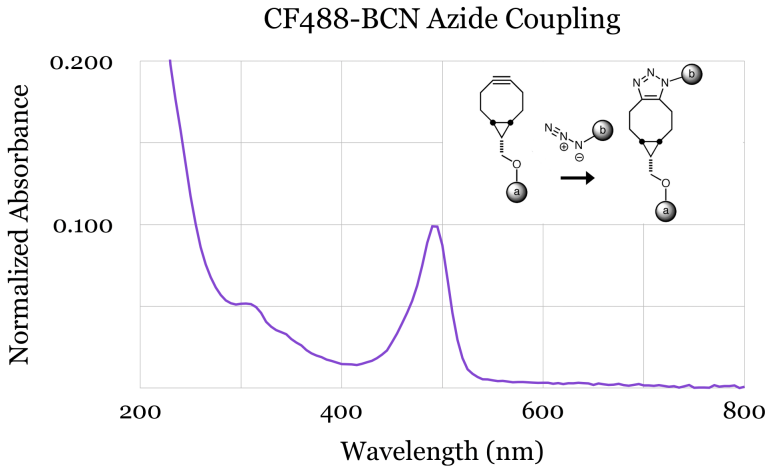

Figure 4.6: Azide to BCN coupling. CF488A-BCN dye was conjugated onto probe exteriors and centrifuge filter washed prior to absorbance spectrometry.

Of particular note, DLS results taken after the addition of MeTz show backfilled probes seem smaller than their counterparts before the addition of MeTz (Fig. 4.3). This might be due to the hydrophobic nature of tetrazine, which could collapse PEG coronas and shield itself even in backfilled conditions.

Prior to Az-DBCO coupling, we tested whether azido groups were both present and exposed via a 1,3-dipolar Huisgen cycloaddition reaction with CF488A-BCN fluorescent labels (Fig. 4.6). After filtered centrifugation tube washes, a strong green-blue color persisted and absorption data revealed the presence of a peak at 488 nm, corresponding with the CF488A dye absorption peak.

After Az-DBCO coupling, we tested whether probes were successfully terminated in MeTz. Cy5-TCO purchased from Click Chemistry Tools, was reacted to probe exteriors via the MeTz-TCO reaction for an hour in the presence of DMF. Subsequent washes via filtered centrifugation tubes produced probes with purple hue, characteristic of Cy5 emission.

These results illustrate silica probes were succcesfully modified and terminated with azido groups on PEG chains, followed by MeTz groups, and were ready to proceed with biomarker targeting. To recap, fully functionalized 40 nm silica probes encapsulated fluorescent species of interest. Silica cores were surrounded by a large PEG corona, comprising entirely of long PEG chains or a combination of long and short backfilled PEG chains. PEGylated probe exteriors terminated in exposed MeTz groups to allow subsequent conjugation onto a TCO-antibody in order to target tumor biomarkers of interest.

Chapter 5

Targeting

Upon complete functionalization, finalized MeTz-probes were ready to commence targeting trials. This was initially conducted via two-step targeting of TCO-modified antibodies onto cell surfaces, followed by addition of probes without backfill, and later by backfilled probes. Lastly, ICs were formed by direct conjugation of antibodies and probes together, followed by direct cell targeting as a single unit. ICs also necessitated SEC to remove aggregates or other large structures from final solutions.

5.1 Bioconjugate Preparation

Three elements are required for two-step targeting; finalized probes, modified antibodies, and cells with a biomarker of interest. To match MeTz termini on probes, appropriate antibodies must be modified with TCO. Among the commonly available amino acid side chains, primary amines on lysine remain the most popular target for antibody modifications [3]. For this specific reaction, the NHS ester to primary amine

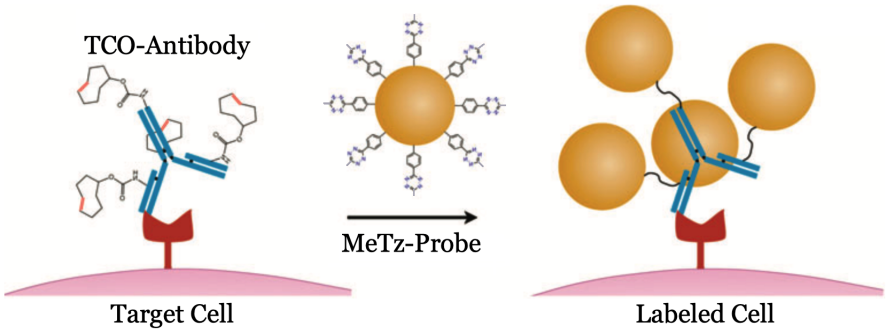

Figure 5.1: During two-step targeting, TCO-modified antibodies first target a select biomarker and are subsequently labeled by a Tz-probe.

reaction from section 3.1 was employed, previously used to couple dye to triethoxy silanes for probe incorporation. TCO-NHS ester, purchased from Click Chemistry Tools, was used for these reactions.

Previous investigations by the Haun Group found TCO groups were often buried within antibodies and inactive, which may be alleviated by using high levels of bovine serum albumin (BSA) in solution [42]. A second method involves conjugating PEG chains onto antibodies via the carbodiimide crosslinker reaction used in section 4.1. For antibody-probe bioconjugation, we employed the use of both TCO linkers directly conjugated to antibodies and TCO-terminated PEGylated antibodies.

For targeting studies, breast cancer cell lines, MCF-7 and SKBR3, were specifically chosen for overexpressing epithelial cell adhesion molecule (EpCAM) and human epidermal growth factor receptor 2 (HER2), respectively. Corresponding antibodies, anti-EpCAM (aEpCAM) and anti-HER2 (aHER2), were purchased from ConjuProbe, modified with TCO or PEG8-TCO, and analyzed with a NanoDrop 2000 system to ensure appropriate concentration.

TCO-NHS ester, stored in DMF, in the presence of phosphate buffered silane (PBS)

and BSA (as PBS+) was used to modify select antibodies at primary amine termini during a 1 hour reaction (see Appendix A.4 for protocol). Alternatively, COOH-PEG8-amine chains, purchased from Click Chemistry Tools, were modified via TCO-NHS to produce COOH-PEG8-TCO, and subsequently coupled to amine termini on antibodies via carbodiimide crosslinking for 3 hours in the presence of NHS and EDC. Fully modified antibodies were stored at 4 C until used for targeting.

5.2 Two-Step Targeting

To commence two-step targeting, tumor cell lines of interest were allowed to grow in cell culture flasks until an appropriate passage number and placed in 8 well borosilicate chamber slides via established American Type Culture Company (ATCC) culture protocols. Cells were allowed to adhere to well plate bottoms and proliferate for another 1-2 days within 500 µL the appropriate culture media as specified by the ATCC. For two-step targeting, media was carefully aspirated out of wells, and followed by three PBS+ washes and aspiration cycles to clear out suspended cellular debris. Modified TCO-antibodies, stored in PBS, were then added to well plates at 10 µg/mL and allowed to attach to biomarkers for 30 minutes. Three additional PBS+ washes followed before the addition of MeTz-Probes at variable nM concentrations, and allowed to react for 1 hour. Three final PBS+ wash cycles were used to remove non-adhered probes and placed in 150 µL of PBS+ (see Appendix A.5 for protocol).

For the first set of targeting experiments, MeTz-probes with only the addition of long PEG chains at varying ratios of AzPEG densities were used. Phasor plot results (Fig. 5.2), illustrate several control and positive conditions at different AzPEG surface

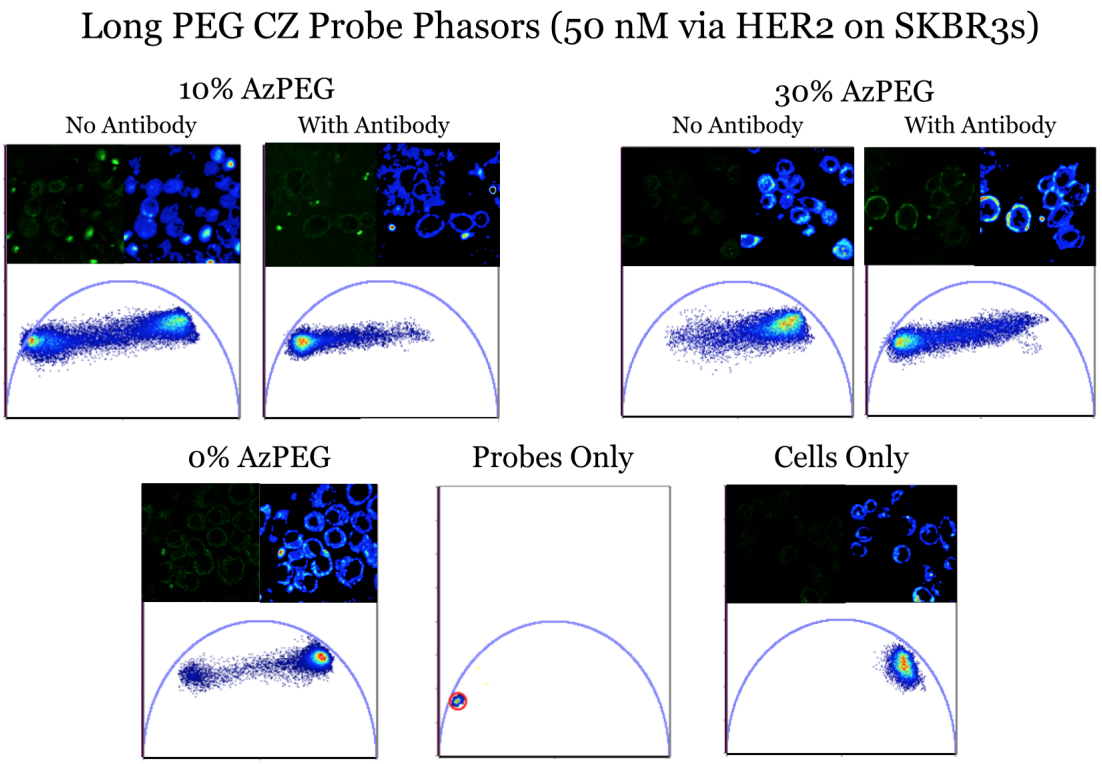

Figure 5.2: Long PEG-modified MeTz-terminated CZ probes targeted onto HER2 in the presence of antibody (positive) and no antibody (control), at different AzPEG densities with probe-only and cell-only controls.

densities. For all experiments shown, probes are excited with a 438 nm excitation laser and imaged in the 560-660 emission window.

While the probes-only control features probes in aqueous solution on a glass slide, the cells-only control features cells adhered to glass on the bottom of a well. Due to various autofluorescent species naturally existing within cells (i.e. NADH and FAD), the cell-only position on the phasor plot corresponds with this intrinsic combination of lifetimes for a given cell type. The 0% AzPEG control features probes that contain no AzPEG, nor any MeTz, and thus lack the ability to specifically bind to antibodies. The remainder of the conditions specify the percent of AzPEG groups compared to total long PEG molecules, which directly correlates with the assumption that one

MeTz molecule was able to bind to a probe for every AzPEG chain. For all variable AzPEG percentages, both a control condition (without any antibody) and a positive condition (with antibody) were tested. Phasor plots contain insets of cell fluorescence images and FLIM images using the phasor approach to generate heat maps of cells.

Phasor positions of no-antibody controls and antibody positives largely correspond with the expected location of probes that were able to successfully bind to biomarkers. However, large aggregate structures are clearly visible in image insets, alongside large prominent tails across phasor plots. This indicates that some level of non-specific targeting, possibly due to aggregates, is present in solution mixtures prior to cell targeting experiments. To circumvent these issues, we subsequently used backfilled MeTz-probes at various densities of long AzPEG (Fig. 5.3).

The phasor plots for these conditions also illustrate similar control and positive results as MeTz-probes with only long PEG chains. Of note, every condition with silica probes produced large amounts of visible aggregates or non-specific binding to glass surfaces. This is further exemplified by similar phasor plots between no-antibody and antibody conditions, indicating PBS wash cycles were not sufficient to remove silica probes from glass slides. The failure of backfilled probes to perform as well as non-backfilled probes might possibly be due to nanoscale imperfections on glass slides which could trap particles due to the differential lengths in PEG chains.

5.3 Immunoconjugation

A potential method to prevent adherence of backfilled probes to glass surfaces could involve an assay of probes modified with different ratios of long PEG to short PEG,

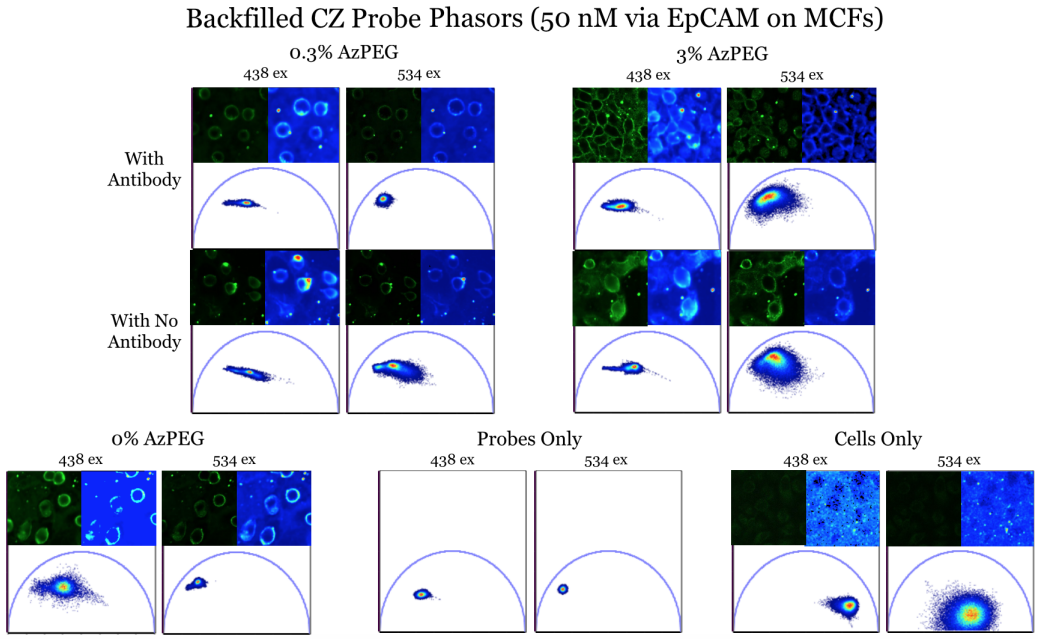

Figure 5.3: Backfilled MeTz-terminated CZ probes targeted onto EpCAM in the presence of antibody (positive) and no antibody (control), at different AzPEG densities with probe-only and cell-only controls.

as our own backfilled modifications have only used a 9:1 ratio. However, this might still not prevent significant aggregation as probes with only long PEG also retained high levels to non-specific binding of large structures. To help circumvent aggregates in our final solutions, ICs were created specifically for allowing SEC to occur after MeTz-TCO coupling. Both types of PEGylated probes, with and without backfilled PEG chains, were conjugated onto antibodies of interest, size-separated through liquid chromatography, and targeted onto biomarkers of interest.

A 4x molar excess of TCO-antibodies were allowed to react with MeTz-probes for 1 hour in the presence of PBS in aqueous solution (see Appendix A.6 for full protocol). After reacting, ICs in PBS solution were filtered through an AKTA pure size exclusion liquid chromatography system connected to an XK 16/40 column packed with Sephacryl S-500 HR resin, purchased from GE Healthcare.

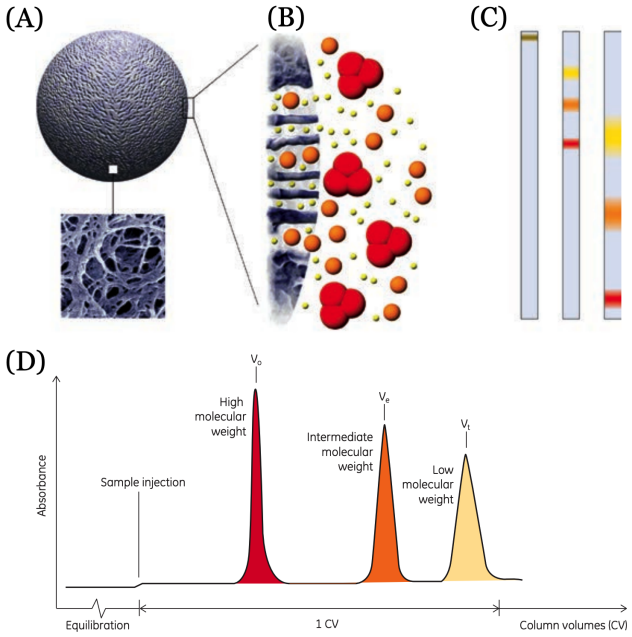

Figure 5.4: (A-B) 50 μm porous beads readily internalize small particles via diffusion. (C-D) Larger particles avoid entry into beads and emerge first from column, while smaller particles emerge later based on size [18].

Initially, particle recovery via fluorometry indicated over 99.9% of probes passed through the column were lost. The high concentration, containing quantum dots, visibly stained the top of the column an orange hue, indicating probes in PBS solution had failed to pass through. Likewise, fluorometry reported over 99.9% of probes had been lost. Unexpectedly however, during column-washing in water after the main filtration and collection sequence, the orange stain disappeared and was sent into waste. This indicated probes in water could pass through a column instead of in PBS.

The stability of probes in different solvents was subsequently tested. In the presence of water particles were stable. However, PBS and PBS+ (PBS and BSA protein) solutions caused irreversible aggregation and sedimentation of particles. We proceeded to compare the stability of particle cores terminated in CEST, TPMP, and a mixture

of CEST and TPMP. Unexpectedly, the CEST-only condition remained stable in all solvents. With the addition of mPEG to CEST-terminated probe cores, probes remained stable in water and PBS+, but still produced large levels of sedimentation in the presence of PBS.

The stability of CEST cores in PBS, when compared to CEST cores modified with mPEG indicates the cohesive repulsion of CEST is masked by mPEG on probes. The known stability of mPEG chains in aqueous and ionic solutions dictates this should not occur if no other destabilizing agents were present. We believe the reason for this instability might be due to residual surfactant left over from reaction synthesis that continues to coat probe surfaces. The removal of this surfactant via incineration of probes at high temperature is a possible way to circumvent this issue. An alternative strategy could include the addition of anionic moieties to PEG chains to help prevent probe aggregation. Thereafter, SEC after immunoconjugation could remove aggregates and promote efficient targeting of biomarkers when analyzed with the phasor approach to FLIM.

Chapter 6

Summary

Tumor heterogeneity has necessitated creation of biomarker detection platforms which can characterize complex microenvironments to help develop successful personalized treatments. However, current large-scale analytical methods typically destroy samples, thereby causing the loss of spatial information and the identification of rare key cell types, which exhibit critical roles in cancer progression. Fluorescent probes may be used to extract this information, however, current libraries retain limits of 5-10 detection channels and alternative probe systems are exceedingly expensive or time-consuming for practical clinical settings. The phasor approach to FLIM has recently provided the potential to expand upon conventional fluorescence imaging by adding an extra dimension of detection channels, but has not yet reached its full potential due to the lack of an existing lifetime probe library.

Here, we have demonstrated the preliminary construction of a lifetime library of probes using silica to encapsulate a controlled mixture of fluorescent species via reverse microemulsion synthesis. Incorporated agents include hydrophobic quantum

dots transferred into probe interiors, and either organic fluorescent or dark quenching dyes, integrated into probe cores. These mixtures have been used to unlock a wide array of phasor positions within the yellow-orange spectral window centered at 590 nm. Bright CdSe/ZnS quantum dot, developed by NN-Labs, were employed as the workhorse fluorescent species for modifications and targeting. Dynamic light scattering and electron microscopy revealed 40 nm probes encapsulating quantum dots. Probe surfaces were further treated with carboxylic acid and phosphonate functional groups, as a basis for further modifications and promotion of aqueous dissolution.

Carbodiimide crosslinking reactions between carboxylic acid domains and primary amines were used to conjugate thousands of PEG chains per probe. These PEG molecules comprised of either long 35 or 36 block chains, or a combination of backfilled 12 block short chains and long chains. While most chains terminated in an nonreactive methoxy group, some had been retrofitted with azide moieties in order to couple DBCO-MeTz linkers via a highly specific bioorthogonal click chemistry reaction. Finalized MeTz-probes could then undergo a second rapid click chemistry reaction by coupling to a premodified TCO-antibody.

TCO-MeTz reactions could either occur in-vitro via two-step targeting or through the formation of immunoconjugates prior to direct targeting. Two-step targeting initially showed non-backfilled probes were able to target biomarkers more effectively than backfilled counterparts, however, large aggregates and non-specific binding of probes was observed. Immunoconjugates were subsequently created and underwent size exclusion chromatography. However, in the presence of protein, aggregation still occurred. Future work will focus on removal of residual surfactant via incineration to prevent protein adsorption. An alternative approach is to load anionic moieties onto probe termini prior to addition of protein.

With this work, we hope to test other probes encapsulating a specific mixture of fluorescent species within our lifetime library in the yellow-orange spectral window. We will then begin multiplexing select immunoconjugates to specific biomarkers of interest, and finally, expand to other windows. Ultimately, we hope to use our lifetime library of probes to help rapidly identify a wide array of key biomarkers in clinical settings in order to help rapidly develop successful personalized treatments via biomarker-targeted therapies.

Bibliography

[1] M. Angelo, S. C. Bendall, R. Finck, M. B. Hale, C. Hitzman, A. D. Borowsky, R. M. Levenson, J. B. Lowe, S. D. Liu, Y. Natkunam, and G. P. Nolan. Multiplexed ion beam imaging (MIBI) of human breast tumors. *Nature Medicine*, 20(4):436–442, 2014.

[2] D. R. Bandura, V. I. Baranov, O. I. Ornatsky, A. Antonov, R. Kinach, X. Lou, S. Pavlov, S. Vorobiev, J. E. Dick, and S. D. Tanner. Mass Cytometry : Technique for real time single cell multitarget immunoassay based on inductively coupled plasma time-of-flight mass spectrometry. *Analytical Chemistry*, 81(16):6813–6822, 2016.

[3] C. R. Behrens, B. Liu, C. R. Behrens, and B. Liu. Methods for site-specific drug conjugation to antibodies Methods for site-specific drug conjugation to antibodies. *mAbs*, 6(1):46–53, 2014.

[4] R. A. Burrell, N. McGranahan, J. Bartek, and C. Swanton. The causes and consequences of genetic heterogeneity in cancer evolution. *Nature*, 501(7467):338–345, 2013.

[5] V. Cauda, C. Argyo, and T. Bein. Impact of different PEGylation patterns on the long-term bio-stability of colloidal mesoporous silica nanoparticles. *Journal of Materials Chemistry*, 20(39):8693–8699, 2010.

[6] K. F. Chou and A. M. Dennis. Förster resonance energy transfer between quantum dot donors and quantum dot acceptors. *Sensors*, 15(6):13288–13325, 2015.

[7] A. H. Clayton, Q. S. Hanley, and P. J. Verveer. Graphical representation and multicomponent analysis of single-frequency fluorescence lifetime imaging microscopy data. *Journal of Microscopy*, 213(1):1–5, 2004.

[8] G. Comito, E. Giannoni, C. P. Segura, P. Barcellos-De-Souza, M. R. Raspollini, G. Baroni, M. Lanciotti, S. Serni, and P. Chiarugi. Cancer-associated fibroblasts and M2-polarized macrophages synergize during prostate carcinoma progression. *Oncogene*, 33(19):2423–2431, 2014.

[9] Q. Dai, C. Walkey, and W. C. W. Chan. Polyethylene glycol backfilling mitigates the negative impact of the protein corona on nanoparticle cell targeting. *Angewandte Chemie - International Edition*, 53(20):5093–5096, 2014.

[10] A. Dehghanghadikolaei, J. Ansary, and R. Ghoreishi. Sol-gel process applications: A mini-review. *Proceedings of the Nature Research Society*, 2(02008), 2018.

[11] N. K. Devaraj, R. Upadhyay, J. B. Haun, and S. A. Hilderbrand. Fast and sensitive pretargeted labeling of cancer cells via tetrazine/trans-cyclooctene cycloaddition. 48(38):7013–7016, 2009.

[12] M. A. Digman, V. R. Caiolfa, M. Zamai, and E. Gratton. The phasor approach to fluorescence lifetime imaging analysis. *Biophysical Journal*, 94(2):14–16, 2008.

[13] E. Elshik, R. Bester, and A. Nel. *Appropriate Solar Spectrum Usage: The Novel Design of a Photovoltaic Thermal System*. University of Johannesburg, 2017.

[14] T. Förster. *Delocalized Excitation and Excitation Transfer*. Florida State University, 1965.

[15] O. Golfetto, E. Hinde, and E. Gratton. Laurdan fluorescence lifetime discriminates cholesterol content from changes in fluidity in living cell membranes. *Biophysical Journal*, 104(6):1238–1247, 2013.

[16] M. Grabolle, P. Kapusta, T. Nann, X. Shu, J. Ziegler, and U. Resch-Genger. Fluorescence lifetime multiplexing with nanocrystals and organic labels. *Analytical Chemistry*, 81(18):7807–7813, 2009.

[17] Q. S. Hanley and A. H. Clayton. AB-plot assisted determination of fluorophore mixtures in a fluorescence lifetime microscope using spectra or quenchers. *Journal of Microscopy*, 218(1):62–67, 2005.

[18] G. E. Healthcare. *Size Exclusion Chromatography Principles and Methods*. 2018.

[19] G. T. Hermanson. *Bioconjugate Techniques 3rd edition*. 2013.

[20] K. Hoffmann, T. Behnke, D. Drescher, J. Kneipp, and U. Resch-Genger. Near-infrared-emitting nanoparticles for lifetime-based multiplexed analysis and imaging of living cells. *ACS Nano*, 7(8):6674–6684, 2013.

[21] M. L. Huggins, P. Rev, and P. April. The crystal structure of quartz. 19(4):363, 1922.

[22] J. Jeevanandam, A. Barhoum, Y. S. Chan, A. Dufresne, and M. K. Danquah. Review on nanoparticles and nanostructured materials: History, sources, toxicity and regulations. *Beilstein Journal of Nanotechnology*, 2018(9):1050–1074, 2018.

[23] I. JM, P. O. Hovland R Fau - Krutzik, O. D. Krutzik Po Fau - Perez, O. Perez Od Fau - Bruserud, B. T. Bruserud O Fau - Gjertsen, G. P. Gjertsen Bt Fau - Nolan, and N. GP. Single cell profiling of potentiated phospho-protein networks in cancer cells. *Cell*, 118(2):217–228, 2004.

[24] S. Jones, W.-d. Chen, G. Parmigiani, F. Diehl, N. Beerenwinkel, T. Antal, A. Traulsen, M. A. Nowak, C. Siegel, V. E. Velculescu, K. W. Kinzler, B. Vogelstein, J. Willis, and S. D. Markowitz. Comparative lesion sequencing provides insights into tumor evolution. *Proceedings of the National Academy of Sciences*, 105(11):4283–4288, 2008.

[25] M. R. Junttila and F. J. De Sauvage. Influence of tumour micro-environment heterogeneity on therapeutic response. *Nature*, 501(7467):346–354, 2013.

[26] K. Kang, J. Park, and E. Kim. Tetrazine ligation for chemical proteomics. *Proteome Science*, 15:15, 2017.

[27] R. Koole, M. M. V. Schooneveld, J. Hilhorst, C. D. M. Donegá, C. Hart, A. V. Blaaderen, D. Vanmaekelbergh, A. Meijerink, and D. C. Hart. On the incorporation mechanism of hydrophobic quantum dots in silica spheres by a reverse microemulsion method. *Chemistry of Materials*, 20(7):2503–2512, 2008.

[28] S. V. Koushik, H. Chen, C. Thaler, H. L. Puhl, and S. S. Vogel. Cerulean, venus, and venusY67C FRET Reference standards. *Biophysical Journal*, 91(12):99–101, 2006.

[29] T. B. Krasieva, C. Stringari, F. Liu, C.-H. Sun, Y. Kong, M. Balu, F. L. Meyskens, E. Gratton, and B. J. Tromberg. Two-photon excited fluorescence lifetime imaging and spectroscopy of melanins in vitro and in vivo. *Journal of Biomedical Optics*, 18(3):031107, 2012.

[30] J. R. Lakowicz. Radiative Decay Engineering: Biophysical and Biomedical Applications. *Analytical Biochemistry*, 298(1):1–24, 2001.

[31] K. Q. Lao, F. Tang, C. Barbacioru, Y. Wang, E. Nordman, C. Lee, N. Xu, X. Wang, B. Tuch, J. Bodeau, A. Siddiqui, and M. A. Surani. mRNA-sequencing whole transcriptome analysis of a single cell on the solid system. *Journal of Biomolecular Techniques*, 20(5):266–271, 2009.

[32] S. Liao, Y. Sun, and U. Coskun. FLIM analysis using the phasor plots. *ISS*, 2014.

[33] C. H. Lin, J. H. Chang, Y. Q. Yeh, S. H. Wu, Y. H. Liu, and C. Y. Mou. Formation of hollow silica nanospheres by reverse microemulsion. *Nanoscale*, 7(21):9614–9626, 2015.

[34] Y. S. Lin, S. H. Wu, C. T. Tseng, Y. Hung, C. Chang, and C. Y. Mou. Synthesis of hollow silica nanospheres with a microemulsion as the template. *Chemical Communications*, 2009(24):3542–3544, 2009.

[35] K. Ma, D. Zhang, Y. Cong, and U. Wiesner. Elucidating the mechanism of silica nanoparticle PEGylation processes using fluorescence correlation spectroscopies. *Chemistry of Materials*, 28(5):1537–1545, 2016.

[36] R. A. Madan, J. L. Gulley, and P. W. Kantoff. Demystifying immunotherapy in prostate cancer: Understanding current and future treatment strategies. *Cancer Journal*, 19(1):50–58, 2013.

[37] A. Mehmood, H. Ghafar, S. Yaqoob, U. F. Gohar, and B. Ahmad. Mesoporous silica nanoparticles: A review. *Journal of Developing Drugs*, 6(2):1000174, 2017.

[38] J. D. Orth, Y. Tang, J. Shi, C. T. Loy, C. Amendt, F. T. Zenke, and T. J. Mitchison. Quantitative live imaging of cancer and normal cells treated with Kinesin-5 inhibitors indicates significant differences in phenotypic responses and cell fate. *Molecular Cancer Therapeutics*, 7(11):3480–3489, 2009.

[39] H. Ow, D. R. Larson, M. Srivastava, B. A. Baird, W. W. Webb, and U. Wiesnert. Bright and stable core-shell fluorescent silica nanoparticles. *Nano Letters*, 5(1):113–117, 2005.

[40] E. Paldino, V. Tesori, P. Casalbore, A. Gasbarrini, and M. A. Puglisi. Tumor initiating cells and chemoresistance: Which is the best strategy to target colon cancer stem cells? *BioMed Research International*, 2014:859871, 2014.

[41] K. T. Pate, C. Stringari, S. Sprowl-Tanio, K. Wang, T. TeSlaa, N. P. Hoverter, M. M. McQuade, C. Garner, M. A. Digman, M. A. Teitell, R. A. Edwards, E. Gratton, and M. L. Waterman. Wnt signaling directs a metabolic program of glycolysis and angiogenesis in colon cancer. *The EMBO Journal*, 33(13):1454–1473, 2014.

[42] M. K. Rahim, R. Kota, and J. B. Haun. Enhancing reactivity for bioorthogonal pretargeting by unmasking antibody-conjugated trans -cyclooctenes. *Bioconjugate Chemistry*, 26(2):352–360, 2015.

[43] M. K. Rahim, R. Kota, S. Lee, and J. B. Haun. Bioorthogonal chemistries for nanomaterial conjugation and targeting. *Nanotechnology Reviews*, 2(2):215–227, 2013.

[44] S. B. Raymond, D. A. Boas, B. J. Bacskai, and A. T. N. Kumar. Lifetime-based tomographic multiplexing. *Journal of Biomedical Optics*, 15(4):046011, 2010.

[45] G. I. Redford and R. M. Clegg. Polar plot representation for frequency-domain analysis of fluorescence lifetimes. *Journal of Fluorescence*, 15(5):805–815, 2005.

[46] R. Rossin, P. R. Verkertk, S. M. Bosch, R. C. M. Vulders, I. Verel, J. Lub, and M. S. Robillard. In vivo chemistry for pretargeted tumor imaging in live mice. *Angewandte Chemie - International Edition*, 2010(14):3375–3378, 2010.

[47] S. Schlücker. SERS microscopy: Nanoparticle probes and biomedical applications. *ChemPhysChem*, 10:1344–1354, 2009.

[48] K. S. Sfanos, T. C. Bruno, A. K. Meeker, A. M. D. Marzo, B. William, and C. G. Drake. Human prostateinfiltrating CD8+ T lymphocytes are oligoclonal and PD1+. *Prostate*, 69(15):1694–1703, 2009.

[49] Q. Shi, L. Qin, W. Wei, F. Geng, R. Fan, Y. Shik Shin, D. Guo, L. Hood, P. S. Mischel, and J. R. Heath. Single-cell proteomic chip for profiling intracellular signaling pathways in single tumor cells. *Proceedings of the National Academy of Sciences*, 109(2):419–424, 2012.

[50] W. Stöber, A. Fink, and E. Bohn. Controlled growth of monodisperse silica spheres in the micron size range. *Journal of Colloid and Interface Science*, 26(1):62–69, 1968.

[51] S. L. Stott, C.-H. Hsu, D. I. Tsukrov, M. Yu, D. T. Miyamoto, B. A. Waltman, S. M. Rothenberg, A. M. Shah, M. E. Smas, G. K. Korir, F. P. Floyd, A. J. Gilman, J. B. Lord, D. Winokur, S. Springer, D. Irimia, S. Nagrath, L. V. Sequist, R. J. Lee, K. J. Isselbacher, S. Maheswaran, D. A. Haber, and M. Toner. Isolation of circulating tumor cells using a microvortex-generating herringbone-chip. *Proceedings of the National Academy of Sciences*, 107(43):18392–18397, 2010.

[52] C. Stringari, A. Cinquin, O. Cinquin, M. A. Digman, P. J. Donovan, and E. Gratton. Phasor approach to fluorescence lifetime microscopy distinguishes different metabolic states of germ cells in a live tissue. *Proceedings of the National Academy of Sciences*, 108(33):13582–13587, 2011.

[53] E. A. Sykes, J. Chen, G. Zheng, and W. C. Chan. Investigating the impact of nanoparticle size on active and passive tumor targeting efficiency. *ACS Nano*, 8(6):5696–5706, 2014.

[54] P. C. Wang. The clonal evolution of tumor cell populations. *Science*, 194(4260):23–28, 1976.

[55] Z. Wang, M. Gerstein, and M. Snyder. RNA-Seq: A revolutionary tool for transcriptomics. *Nature Reviews Genetics*, 10(1):57–63, 2009.

[56] R. H. Wilson, K. P. Nadeau, F. B. Jaworski, B. J. Tromberg, and A. J. Durkin. Review of short-wave infrared spectroscopy and imaging methods for biological tissue characterization. *Journal of Biomedical Optics*, 20(3):030901, 2015.

[57] N. G. Zaorsky, T. M. Churilla, B. L. Egleston, S. G. Fisher, J. A. Ridge, E. M. Horwitz, and J. E. Meyer. Causes of death among cancer patients. *Annals of Oncology*, 28(2):400–407, 2017.

[58] C. L. Zavaleta, B. R. Smith, I. Walton, W. Doering, G. Davis, B. Shojaei, M. J. Natan, and S. S. Gambhir. Multiplexed imaging of surface enhanced Raman scattering nanotags in living mice using noninvasive Raman spectroscopy. *Proceedings of the National Academy of Sciences of the United States of America*, 106(32):13511–13516, 2009.

Appendix A

Procedures

A.1 Reverse Microemulsion Synthesis

1) Add 10 mL of cyclohexane to a vial.

2) Add 1.3 mL of IGEPAL CO-520 to vial using syringe.

3) Add a magnetic stir bar then sonicate until clear.

4) Add quantum dots (QDs) while on stir plate (skip to step 6 if not using QDs)*.

5) Sonicate for 5 minutes.

6) Add dye-silane while on stir plate (skip to step 8 if not using dye-silane)*.

7) Sonicate for 5 minutes.

8) Add 150 μL of ammonia while on stir plate.

9) Sonicate for 1 minute.

10) Add 80 μL of TEOS while on stir plate.

11) Leave on stir plate for 24 hours.

12) Add 2 μL of CEST while on stir plate.

13) Add 1 μL of TPMP while on stir plate.

14) Leave on stir plate for 24 hours.

15) Place 1 mL of sample solution in microcentrifuge tube.

16) Add 0.5 mL of ethanol to tube.

17) Centrifuge at 11,500 rcf for 15 minutes. Remove supernatant.

18) Add 1 mL of ethanol and sonicate until dissolved.

19) Repeat steps 17 - 18 three times, add 1 mL of ultrapure water on last wash.

20) Sonicate until dissolved and store sample at room temperature.

* The amounts of quantum dots or dye-silane can be variable. Unless otherwise specified, we used 200 μL of CZ quantum dots (5 mg/mL in toluene) from NN-Labs.

A.2 Carbodiimide Crosslinker PEGylation

1) Perform calculations to determine reaction volumes.

2) Prepare ultrapure water, EDC, NHS, and PEG stock solutions. Vortex.

3) In microcentrifuge tube combine SNPs, Water, EDC, and NHS. Vortex.

4) Add PEGs to reaction mixture. Vortex and sonicate.

5) Incubate on nutator at room temperature for 3 hours. Sonicate every 20 minutes.

6) Transfer to Amicon Centrifugal Filter (100 kD) and add water to top off.

7) Centrifuge at 2000 rcf for 10 minutes. Remove follow through and add water.

8) Repeat three times. Add desired volume of water after last wash.

9) Sonicate until dissolved and store sample at room temperature.

A.3 Methyltetrazine Linker Conjugation

1) Perform calculations to determine reaction volumes.

2) Prepare ultrapure water, DMF, and MeTz-DBCO stock solutions. Vortex.

3) In microcentrifuge tube combine SNPs, Water, and DMF. Vortex.

4) Add MeTz-DBCO to reaction mixture. Vortex and sonicate.

5) Incubate on nutator at room temperature for 24 hours.

6) Transfer to Amicon Centrifugal Filter (100 kD) and add water to top off.

7) Centrifuge at 2000 rcf for 10 minutes. Remove follow through and add water.

8) Repeat three times. Add desired volume of water after last wash.

9) Sonicate until dissolved and store sample at room temperature.

A.4 Trans-Cyclooctene Antibody Modification

1) Perform calculations to determine reaction volumes.

2) In microcentrifuge tube combine PBS, sodium bicarbonate, and antibody. Vortex.

3) Add DMF and NHS-TCO to solution. Vortex.

4) Incubate on nutator at room temperature for 3 hours.

5) To exchange buffer in Ziba Column, add 1 mL PBS slowly over column bed.

6) Centrifuge at 1000 rcf for 3 minutes. Remove follow through and add water.

7) Add 1 mL of water after last wash and obtain concentration with NanoDrop.

8) Store sample at 4 C.

A.5 Biomarker Targeting

1) Perform calculations to determine reaction volumes.

2) After cells are sufficiently confluent, carefully aspirate media from well.

3) Add with 500 μL of PBS+ and carefully aspirate. Repeat twice.

4) Add TCO-antibodies or TCO-ICs in 150 μL PBS+. Incubate for 30 minutes.

5) Add with 500 μL of PBS+ and carefully aspirate. Repeat twice.

6) Add MeTz-probes in 150 μL PBS+. Incubate for 1 hour (skip if only using ICs).

7) Add with 500 μL of PBS+ and carefully aspirate. Repeat twice.

8) Add 150 μL PBS+. Analyze with phasor approach to FLIM.

A.6 Immunoconjugation

1) Perform calculations to determine reaction volumes.

2) In microcentrifuge tube combine PBS+, and modified antibody. Vortex.

3) Add Tz-probes to reaction solution. Vortex.

4) Incubate on nutator at room temperature for 1 hour.

5) Purify immunoconjugates using HPLC, S-400 or S-500 column.

6) Concentrate product in Amicon Centrifugal Filter (100 kD).

7) Store sample at 4 C.

Appendix B

Calculations

B.1 Probe Count

$$\text{vol}_{QD} = 200\ \mu L \qquad vol_{QD\ stock} = 5000\ \mu L \qquad M_{QD\ stock} = 5.0\ \mu M$$

$$\text{mol}_{QD\ stock} = \frac{5.0\ \mu mol}{L} * 0.005\ L = 25\ nmol$$

$$\text{mol}_{QDs\ in\ rxn} = mol_{QD\ stock} * \frac{200\ \mu L}{5000\ \mu L} = 1.0\ nmol$$

$$\text{number}_{QDs\ in\ rxn} = mol_{QDs\ in\ rxn} * \frac{6.022 * 10^{23}\ molecules}{1\ mol} \approx 6.0 * 10^{14}\ QDs$$

At 1 QD per Probe $\approx 6.0 * 10^{14}$ *Probes per reaction*

B.2 Surface Moieties

$$\text{Silicon Distance}_{cryst} = 0.323\,nm \qquad \rho_{amorph} = 2.196\,\tfrac{g}{mL} \qquad \rho_{cryst} = 2.648\,\tfrac{g}{mL}$$

$$\text{Silicon Distance}_{amorph} = 0.323\,nm * \left(\frac{2.196\,\frac{g}{mL}}{2.648\,\frac{g}{mL}}\right)^{-1} = 0.388\,nm$$

$$\text{Silicon Distance}^2_{amorph} = (0.388\,nm)^2 = 0.152\,nm^2$$

$$\text{Silicon Atoms per nm}^2 = \tfrac{1}{0.152} \approx 6.58$$

$$\text{Surface Area} = 4\pi(\tfrac{40\,nm}{2})^2 = 5026\,nm^2$$

$$\text{Bind sites per Probe} = 5026\ \text{nm}^2 * 6.58\,\tfrac{sites}{nm^2} \approx 33070$$

$$\text{CEST: } 2\,\mu L\ * \tfrac{1}{10^3}\tfrac{mL}{\mu L} * \tfrac{1.170}{1}\tfrac{g}{mL} * \tfrac{1}{196.4}\tfrac{mol}{g} * 0.25\,wt\% = 2.983 * 10^{-6}\,mol$$

$$\text{TPMP: } 1\,\mu L\ * \tfrac{1}{10^3}\tfrac{mL}{\mu L} * \tfrac{1.252}{1}\tfrac{g}{mL} * \tfrac{1}{238.2}\tfrac{mol}{g} * 0.50\,wt\% = 2.628 * 10^{-6}\,mol$$

$$\text{CEST per Probe} \approx 33070\,sites * \left(\tfrac{2.983}{2.983+2.628}\right) \approx 17580$$

$$\text{Estimated PEG per nm}^2 \approx 6.0 \quad [9]$$

$$\text{Max PEG per Probe} \approx \tfrac{6.0}{6.58} * 17580 \approx 16040$$